AIAA JOURNAL
Vol. 30, No. 4, April 1992

Solution-Adaptive Grid Procedure for the Parabolized Navier-Stokes Equations

Albert D. Harvey III* and Sumanta Acharya†
Louisiana State University, Baton Rouge, Louisiana 70803
and
Scott L. Lawrence‡
NASA Ames Research Center, Moffett Field, California 94035

A solution-adaptive grid procedure based on an error equidistribution principle is developed and applied to a three-dimensional parabolized Navier-Stokes solver. The scheme redistributes grid points line by line in both crossflow directions, with grid point motion controlled by forces analogous to tensional and torsional spring forces. The tensional force is proportional to the error measure or a weighting function related to the error measure. The torsional force is used to control grid skewness relative to the upstream and cross-stream coordinate lines. Weighting functions are selected by first normalizing flowfield gradients and/or curvature of a number of dependent variables and then selecting the largest at each point. The hypersonic flow over a right-circular cone at three different yaw angles is studied to demonstrate the performance of the solution-adaptive grid procedure. Pitot pressure profiles and surface pressure computed using the solution-adaptive algorithm are compared with experimental results as well as with numerical results obtained using a fixed grid. Pitot pressure predictions using the adaptive grid algorithm show better agreement with experiment than those obtained using a fixed grid.

Introduction

In recent years, increasing attention has been focused on techniques for constructing an optimal numerical grid surrounding the region of interest. A useful grid must provide clustering in high error regions such as boundary layers and around shock waves in order to sufficiently resolve these features. The use of solution-adaptive gridding enables the grid and the solution to the field equations to evolve simultaneously. As the solution process converges toward a fixed state, the grid continually adjusts to the evolving flowfield features, clustering mesh points in regions containing high solution error.

The present work involves a solution-adaptive grid scheme for the three-dimensional parabolized Navier-Stokes (PNS) equations. Solutions using the PNS equations are obtained by spatially advancing the solution in the marching direction between constant cross-stream surfaces. The first step in the solution-adaptive process is to obtain an initial solution on the cross-stream surface corresponding to the present marching station. Using this preliminary solution, the mesh is adapted in both cross-stream directions, clustering grid points in regions of high flowfield gradients and/or curvature. A refined solution is then obtained by remarching the PNS solver across the newly adapted surface. The adapted mesh is projected downstream to the next marching station where it is used to obtain a preliminary solution; then this process is repeated.

Thompson[1] and Hawken[2] provide excellent reviews on current solution-adaptive grid techniques. The method adopted in the present work to redistribute grid points is similar to the method of Nakahashi and Deiwert[3,4] in which grid point motion is controlled by forces analogous to tensional and torsional springs set between grid points. The tensional forces are a function of the local error measure or weighting function. The torsional forces relate adjacent grid lines and prevent relative grid skewness. This method is actually an extension of the method first introduced by Gnoffo[5] and has been used successfully by Davies and Venkatapathy[6] and Djomehri and Deiwert.[7]

The solution-adaptive technique used in the present work is an extension of the two-dimensional line-by-line solution-adaptive technique of Harvey et al.[8] in which only one crossflow direction exists. In extending these ideas of a two-dimensional parabolic adaptation routine to a three-dimensional one, a number of contention issues arise. For example, to control grid skewness, the torsional force from the upstream grid line and that from the neighboring crossflow coordinate line may dictate opposing grid point motion. Grid adaptation may require excessive point motion, causing the grid to move too rapidly and become skewed. As a result, the second solution step of the solution-adaptive procedure becomes unstable. The grid must be allowed to move only within prescribed bounds at each marching station. A new method of formulating skewness control criteria is introduced in this paper that disallows abrupt and excessive grid point movement so as to permit an uninterrupted second solution step on a uniform computational slab.

Solutions using the PNS equations are obtained by marching in space rather than time and are therefore obtained much more efficiently than solutions employing the time-dependent Navier-Stokes equations. The present PNS solver, developed by Lawrence,[9,10] applies upwinding to the parabolized Navier-Stokes equations using a steady version of Roe's[11] approximate Riemann solver to model the inviscid crossflow numerical fluxes.

The following section contains a brief description of the PNS solver. Later sections describe the grid adaptation procedure and present some numerical results obtained using the solution-adaptive parabolized Navier-Stokes solver.

Flow Algorithm

The present flow solver involves the integration of the PNS equations, which incorporates a steady version of Roe's approximate Riemann solver for the modeling of the inviscid

Received Jan. 2, 1991; revision received June 17, 1991; accepted for publication July 6, 1991.

*Research Assistant, Mechanical Engineering; currently, Senior Research Engineer, Dow USA Research and Development. Member AIAA.
†Professor, Mechanical Engineering. Member AIAA.
‡Research Scientist. Member AIAA.

fluxes. The PNS equations are obtained from the steady-state Navier-Stokes equations by neglecting streamwise viscous derivatives and by separating the portion of the streamwise pressure gradient term that is responsible for introducing ellipticity into the equation. These equations can be written with respect to a generalized coordinate system as

$$\frac{\partial \bar{E}^*}{\partial \xi} + \frac{\partial \bar{E}^p}{\partial \xi} + \frac{\partial \bar{F}}{\partial \eta} + \frac{\partial \bar{G}}{\partial \zeta} = 0 \tag{1}$$

The ξ coordinate is defined as the streamwise direction, and η and ζ are the crossflow directions. The quantities $\bar{F}$ and $\bar{G}$ represent the crossflow numerical fluxes in the η and ζ directions, respectively. The superscript asterisk denotes the omission of streamwise viscous derivatives. The terms $\bar{E}^*$ and $\bar{E}^p$ are the result of employing the Vigneron technique[12] to split the streamwise flux vector. They are defined by

$$\bar{E}^* = \begin{bmatrix} \rho\hat{U} \\ \rho u\hat{U} + (\xi_x/J)\omega p \\ \rho v\hat{U} + (\xi_y/J)\omega p \\ \rho w\hat{U} + (\xi_z/J)\omega p \\ (E_t + p)\hat{U} \end{bmatrix}, \qquad \bar{E}^p = \begin{bmatrix} 0 \\ (\xi_x/J)(1-\omega)p \\ (\xi_y/J)(1-\omega)p \\ (\xi_z/J)(1-\omega)p \\ 0 \end{bmatrix}$$

with

$$\hat{U} = \left(\frac{\xi_x}{J}\right)u + \left(\frac{\xi_y}{J}\right)v + \left(\frac{\xi_z}{J}\right)w$$

The vector $\bar{E}^*$ is the resultant streamwise flux, and $\bar{E}^p$ is the portion of the original streamwise flux responsible for introducing ellipticity into the equations through the subsonic boundary layer. It is shown in Ref. 12 that Eq. (1) is hyperbolic-parabolic with respect to the dependent vector $\bar{E}^*$, provided that ω satisfies the relation

$$\omega = \min\left[1, \frac{\sigma\gamma M_\xi^2}{1 + (\gamma - 1)M_\xi^2}\right]$$

where M_ξ is the Mach number in the ξ-coordinate direction and σ is a safety factor used to account for nonlinear effects.

Equation (1) is differenced in a conservative manner using finite volumes. An upwind differencing scheme is used that evaluates the inviscid fluxes in the crossflow directions through the solution to a steady version of Roe's approximate Riemann problem with flow properties averaged at cell interfaces using standard Roe averaging (see Ref. 11). This results in a first-order-accurate inviscid flux, which is then extended to second-order accuracy following the approach of Chakravarthy and Szema[13] in which a second-order generic numerical flux is defined in terms of the first-order flux and antidissipative correction terms. The added terms are limited relative to one another in order to eliminate the oscillatory nature that is characteristic of second-order schemes.

The algorithm is made implicit by evaluating the first-order numerical flux at the $n + 1$ marching station and by lagging the second-order correction terms at the nth marching station. A conventional linearization in ξ is then performed and the resulting system of algebraic equations is approximately factored to produce an alternating direction implicit (ADI) scheme.

Adaptation Algorithm

Adaptation Strategy

The method adopted in the present work for redistributing mesh points at each cross-stream grid surface is analogous to minimizing the energy in a system of tension springs set between grid points (see Ref. 5). The tension forces are functions of an error measure that are represented by gradients and/or curvature of a selected dependent flowfield variable. In an effort to reduce grid skewness, this concept was extended by Nakahashi and Deiwert[3,4] to include dependence from neighboring grid points. This additional dependence is analogous to the application of torsion springs set between grid lines or surfaces. For the sake of computational efficiency and simplicity, the analogy is applied along each coordinate line separately. In this manner, the three-dimensional grid point redistribution process is broken into a sequence of unidirectional adaptations along each fixed coordinate line in each of the two crossflow directions. The resulting system of equations for the final grid point positions along each successive coordinate line is tridiagonal and can be efficiently solved.

The grid adaptation technique just described is essentially an error equidistribution method and involves the redistribution of grid points such that an error measure represented by a positive weighting function w_i is equally distributed over a coordinate line,

$$w_i \Delta s_i = K \tag{2}$$

where w_i is the weighting function based on flow properties, and in the terminology of Refs. 4 and 6, it represents the spring constant with K as the resultant force. The grid interval Δs_i is defined as the distance between adjacent nodal points along a line of constant computational coordinate.

The weighting function w_i is defined as a function of a selected normalized flow property $\bar{f}$ such that

$$w_i = 1 + A\bar{f}_i^B \tag{3}$$

where A and B are constants related to the specified maximum and minimum grid spacings. From Eq. (2), the maximum and minimum allowable grid spacing occur when w_i is at its minimum and maximum values, respectively. Since the normalized flow property $\bar{f}$ varies from zero to unity, Eq. (3) states that $w_{\max} = 1 + A$ and $w_{\min} = 1$. Substituting these values into Eq. (2) and rearranging yields $A = \Delta s_{\max}/\Delta s_{\min} - 1$, where $\Delta s_{\max}$ and $\Delta s_{\min}$ are user specified maximum and minimum allowable grid spacings. The constant B of Eq. (3) is chosen so that the computed minimum grid spacing corresponds to $\Delta s_{\min}$, the requested minimum grid spacing. Davies and Venkatapathy[6] outline an iterative procedure for obtaining an approximate value for B. The choice of the normalized flow property $\bar{f}$ is described in the following section.

Summing both sides of Eq. (2), solving for K, then substituting the result for K back into Eq. (2) yields

$$\Delta s_i = s_{\max} \Big/ \left(w_i \sum_{l=1}^{n} \frac{1}{w_l}\right) \tag{4}$$

where $s_{\max}$ is the total length of the coordinate line. This yields the new grid point locations based on local flow properties. Thus, where the weighting function w_i is large, Δs_i will turn out to be small and, therefore, the local truncation error at a point, whose leading term is proportional to $w_i(\Delta s_i)^n$, will tend to be equidistributed over the complete domain.

If Eq. (4) is used alone to determine the new grid spacing along each grid line, the grid will quickly become skewed due to the lack of dependence from surrounding grid lines. To ensure a smoother grid, there needs to be a relationship between the current grid adaptation line (where the grid adaptation is to be performed) and the previously adapted grid line. A torsional spring analogy is introduced to accomplish this task. This procedure relates grid points along adjacent grid lines, thus providing for a smoother grid. For each grid point along the current adaptation line, the present work incorporates torsional dependence from two different directions. One torsion spring extends from the adjacent coordinate line directly upstream of the current adaptation line and the other torsional influence is projected from the neighboring grid point in the crossflow direction. To distinguish between

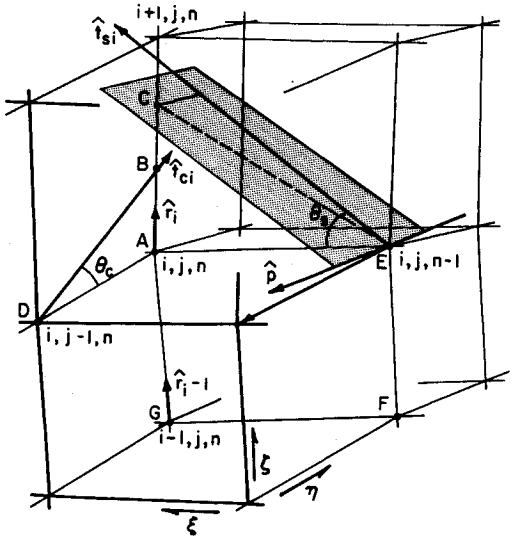

Fig. 1 Three-dimensional adaptive mesh geometry.

the two, subscript s denotes streamwise torsional quantities, whereas subscript c denotes quantities involving crossflow torsional dependence. Using this notation and performing a force balance along a constant ζ line on the resulting system of tensional and torsional springs about the point i,j in Fig. 1, the following system of equations is obtained:

$$w_i(s_{i+1} - s_i) - w_{i-1}(s_i - s_{i-1}) - K_{si}\theta_{si} - K_{ci}\theta_{ci} = 0 \qquad (5)$$

where s_i is the length of the current adaptation line up to the point i,j in Fig. 1 and K_{si} and K_{ci} are proportionality constants. The torsion angles θ_{si} and θ_{ci} can be approximated using the notation of Fig. 1 as $\theta_{si} \approx (s_i - s_{si}')/|EC|$ and $\theta_{ci} \approx (s_i - s_{ci}')/|DB|$. The quantity s_{si}' is defined as the total length of the coordinate line up to the location of its intersection with the streamwise torsion vector $\hat{t}_{si}$. This point corresponds to point C in Fig. 1. The quantity s_{ci}' is defined similarly and is the corresponding intersection point of the crossflow torsion vector $\hat{t}_{ci}$ with the current adaptation line, and is denoted in Fig. 1 by the point B. By substituting these expressions for θ_{si} and θ_{ci} into Eq. (5) and by rearranging and defining $\tau_{si} = K_{si}/|EC|$ and $\tau_{ci} = K_{ci}|DB|$, the following linear system is obtained:

$$w_{i-1}s_{i-1} - (w_{i-1} + w_i + \tau_{si} + \tau_{ci})s_i + w_i s_{i+1}$$
$$= -(\tau_{si}s_{si}' + \tau_{ci}s_{ci}') \qquad (6)$$

Calculation of Torsional Parameters

Equation (6) indicates that, as the terms τ_{si} and τ_{ci} become large, the equilibrium position of the ith point approaches the position corresponding to a weighted average of s_{si}' and s_{ci}'. These two quantities represent the equilibrium positions of the individual torsional springs projecting from neighboring grid lines, denoted by the vectors $\hat{t}_{si}$ and $\hat{t}_{ci}$, respectively, in Fig. 1. Thus, if $\tau_{si} = \tau_{ci}$ and both are much larger than the remaining terms of Eq. (6), the resulting solution to Eq. (6) becomes $s_i = \frac{1}{2}(s_{si}' + s_{ci}')$. Consequently, values of s_{si}' and s_{ci}' much different from s_i, the initial grid positions, can result in excessive movement of grid points, even without any input from the error measure. In the present work, to prevent excessive skewing, large changes in the grid point positions are not desired since a new solution is obtained on the updated grid surface immediately after grid adaptation. Initially, before adaptation and during the preliminary solution process, the downstream side of the computational slab at the nth or current marching station is simply a proportional duplicate of the upstream side. After adaptation, these two sides of the computational slab should not differ too severely from each other to permit an improved solution during the remarching step of the solution-adaptive procedure. If excessive skewing occurs, the solution process becomes unstable. What is desired is that for even larger values of τ_{si} and τ_{ci}, the grid continually retains the smoothness necessary for the solution on the adaptive grid. Previous work using the current grid adaptation method has not reported the stability and accuracy link between the grid skewness and the solution on the adapted grid. To achieve the precise and bounded movement required in the present solution-adaptive scheme, the values of s_{si}' and s_{ci}' must remain close to the preliminary grid point positions, and at the same time, the values of τ_{si} and τ_{ci} of Eq. (6) must be chosen so as to hold the grid close to these locations. Only a small range of the torsion terms will accomplish the latter part of this task. Values of τ_{si} and τ_{ci} too large will smother the effect of the weighting functions, causing the grid to move independent of the solution, whereas values that are too small permit excessive movement. Davies and Venkatapathy[6] assumed the constants K_{si} and K_{ci} of Eq. (5) to be a function of the maximum weighting function and the grid cell face aspect ratio. This procedure was adopted by Harvey et al.[8] However, in some cases, the cell face aspect ratio can vary by several orders of magnitude and, as a result, can produce unpredictable variations in the torsion terms. Djomehri and Deiwert[7] assumed that the torsion terms are proportional to an average value of the weighting functions along the adaptation line. Using this assumption, the resulting values of the torsion terms were found to vary inconsistently from the remaining terms of Eq. (6) at each point.

In the present work, a somewhat different approach is adopted. First, to make all of the terms of Eq. (6) equal in magnitude at each point along the adaptation line, a stiffness parameter Ω_i is defined in the following manner:

$$\Omega_i = \lambda(w_{i-1} + w_i)\bar{\alpha}_i$$

where λ is a user defined stiffness safety factor and is generally given numerical values between 10^{-1} and 10, and $\bar{\alpha}_i = \alpha_i/\alpha_{\min}$ is the aspect ratio of the grid cell normalized with respect to the minimum cell aspect ratio. Each aspect ratio is computed using the notation of Fig. 1 as follows:

$$\alpha_i = \frac{s_{i+1,j,n} - s_{i-1,j,n}}{|DB|}$$

The value of Ω_i is then divided into streamwise and crossflow components according to the lengths of the streamwise and crossflow torsion springs, $|EC|$ and $|DB|$, respectively:

$$K_{si} = \frac{|DB|}{|EC| + |DB|}\Omega_i, \qquad K_{ci} = \frac{|EC|}{|EC| + |DB|}\Omega_i$$

The quantities $|EC|$ and $|DB|$ are the lengths of the streamwise and crossflow torsion springs, respectively. Substituting these expressions for the proportionality constants K_{si} and K_{ci} into the definitions for τ_{si} and τ_{ci} given earlier, the following expressions are obtained:

$$\tau_{si} = \frac{|DB|}{|EC| + |DB|}\frac{\Omega_i}{|EC|}, \qquad \tau_{ci} = \frac{|EC|}{|EC| + |DB|}\frac{\Omega_i}{|DB|} \qquad (7)$$

The use of Eqs. (7) in Eq. (6) ensures that all terms of Eq. (6) are of the same magnitude for all points along the line. When the length of the streamwise torsion spring $|EC|$ is equal to the length of the crossflow torsion spring $|DB|$, then the torsional influence is distributed in the two directions equally and, as a result, equal consideration is given to both equilibrium positions s_{si}' and s_{ci}'. When the two springs are of unequal length (i.e., one grid line is closer to the current adaptation line than the other), more torsional dependence develops from the closer of the two neighboring grid lines. Another advantage of defining the torsion terms in this man-

ner is that a single parameter λ is involved. Other formulations of the torsion terms investigated by the present authors required the introduction of torsion parameters in each of the two directions. As a result, two parameters were required, both of which exhibited a strong dependence on the relative grid scales. To the contrary, the single parameter λ in the present work was found to be relatively insensitive to the scale of the grid due to the balance maintained in the magnitude of the terms of Eq. (6).

A problem in the formulation for the torsional influence arises when adapting the first grid line of each crossflow plane. This grid line does not have a crossflow neighbor. One method of resolving this problem is to temporarily divert all of the torsional dependence to the streamwise direction. This procedure was found to introduce grid irregularities along the boundaries. Another method that is used in the present paper and provides increased grid continuity throughout is to reflect the grid line on the opposite side of this first line to its other side, providing a means of crossflow support to the grid points along the initial line at each marching station.

Determination of Reference Locations

A method of selecting s_{si}' and s_{ci}' is now presented that prevents these quantities from varying significantly from s_i, the initial grid point positions, so that grid skewness is prevented using the values of τ_{si} and τ_{ci} formulated earlier. These quantities are selected in a manner so as to preserve the information that s_{si}' and s_{ci}' should contain concerning the direction in which the grid should move. If the ith torsion vectors $\hat{t}_{si}$ and $\hat{t}_{ci}$ are allowed to cross the current adaptation line at positions greater than the point $i+1,j,n$ or less than $i-1,j,n$ of Fig. 1, then, for sufficiently high values of τ_{si} and τ_{ci}, the grid can become unacceptably distorted. The quantities s_{si}' and s_{ci}' should represent the positions the ith grid point must take in order that the grid acquire the desired amounts of straightness and orthogonality in the streamwise and crossflow directions. If, before adaptation, the initial distribution of grid points does not comprise a grid that is as straight or orthogonal as desired, the amount of point movement needed to obtain these characteristics may exceed the amount of movement that can be tolerated by the second solution step. Thus, to provide a more useful solution-adaptive scheme, grid point motion must be further limited, allowing only incremental movement at each marching station and not permitting straightness and orthogonality constraints to be satisfied too rapidly.

The torsional reference vectors $\hat{t}_{si}$ and $\hat{t}_{ci}$ are constructed from grid orthogonality and straightness vectors. For example, the crossflow torsion vector $\hat{t}_{ci}$ is then defined as

$$\hat{t}_{ci} = C_c \hat{s}_{ci} + (1 - C_c)\hat{n}_{ci} \tag{8}$$

In Eq. (8), the vector $\hat{n}_{ci}$ represents local grid orthogonality and is computed as an average of the normal to the current grid line and the normal to the adjacent grid line in the crossflow direction. The vector $\hat{s}_{ci}$ is a measure of local grid straightness and is computed as the vector from the point $i,j-2,n$ to the point $i,j-1,n$ (point D of Fig. 1). The constant C_c can range from zero to unity and represents the proportion of grid orthogonality to straightness restrictions imposed on the equilibrium position of the torsional springs in the crossflow direction. A value close to zero enforces more orthogonality, whereas values closer to unity provide more grid straightness. As before, subscript c of Eq. (8) denotes crossflow quantities. The straightness vector in the streamwise direction $\hat{s}_{si}$ is computed as the vector from the point $i,j,n-2$ to the point $i,j,n-1$ of Fig. 1 and is used in a similar formulation for $\hat{t}_{si}$, the streamwise torsion vector.

If a torsional reference vector is allowed to cross outside the bounds of the points $i-1,j,n$ and $i+1,j,n$ of Fig. 1, then a situation arises whereby grid points can either cross one another or become severely skewed. To remedy this potential problem, each torsion vector $\hat{t}_i$ is limited so that its intersection point is within $\frac{1}{2}\Delta s_i$ of s_i (or $\frac{1}{2}\Delta s_{i-1}$, depending on which side of the ith point $\hat{t}_i$ crosses). This imposes further limitations on grid point motion, and a greater range of values for τ_{si} and τ_{ci} exists for which the remarching step of the solution-adaptive scheme remains stable.

There is no guarantee that $\hat{t}_{si}$ will intersect the current adaptation line at all, and in general, it rarely does. To assign an approximate value to s_{si}', the vector $\hat{t}_{si}$ is projected onto the current adaptation line in a manner that will preserve the information concerning grid characteristics supplied by the values of s_{si}' and s_{ci}'. The shaded plane in Fig. 1 is the plane containing the torsion vector $\hat{t}_{si}$ and a vector denoted as $\hat{p}$, which is taken as the normal to $\hat{t}_{si}$ and $\hat{r}_k$, a unit vector in the direction of the current line segment. The index k denotes either i or $i-1$, depending on whether $\hat{t}_{si}$ subtends above or below, respectively, of the ith point along the current adaptation line (point A of Fig. 1). Point C is then found to be the point where $\hat{r}_k$ intersects the plane of $\hat{t}_{si}$ and $\hat{p}$. As mentioned earlier, the distance $|AC|$ is limited to a maximum value of $\frac{1}{2}\Delta s_k$, and if it exceeds this value, it is reset to $\frac{1}{2}\Delta s_k$.

For the present work, a constant ξ surface corresponds to a constant x plane in physical space, which is planar, and the line segments $|DB|$ and $|AB|$ are easily found from the simultaneous solution of the y and z components of the following vector equation:

$$|DB|\hat{t}_{ci} = \hat{DA} + |AB|\hat{r}_k$$

where $\hat{DA}$ is a vector from point D to point A of Fig. 1, $\hat{t}_{ci}$ and $\hat{r}_k$ are unit vectors in the indicated directions, and as before, the index k denotes i or $i-1$, depending on whether $\hat{t}_{ci}$ crosses above or below the ith point. In general, the planar assumption is not required, and if not present, a three-dimensional analysis similar to that described earlier for evaluating $\hat{t}_{si}$ would be needed to evaluate the intersection point of $\hat{t}_{ci}$ and $\hat{r}_k$. To further limit point movement and increase the stability of the improved solution step for a wider range of τ_{ci}, the distance $|AB|$ of Fig. 1 is also limited to $\frac{1}{2}\Delta s_k$.

Once the points B and C of Fig. 1 are located, s_{si}' and s_{ci}' are computed as the arc length of the adaptation line up to these points. These values of s_{si}' and s_{ci}' provide Eq. (6) with an additional force acting on the grid points, pulling them in the direction they must move in order that grid straightness and orthogonality requirements must be satisfied. Equation (6) is tridiagonal, and can then be solved easily for s_i, the final grid point positions. This is done in an iterative manner, interpolating the weighting functions at each iteration until the grid becomes stationary.

Adaptation Boundaries

The adaptation domain, in the present work, can include all or be a subset of the entire solution domain. Special procedures are necessary at the boundaries of the adaptation domain so as to allow a smooth transition of the grid into the adaptation domain. At each adaptation line, a specified edge spacing Δs_{edge} is defined as either a required wall spacing if the adaptation domain is adjacent to a solid boundary or as the grid spacing immediately outside the adaptation domain if it is a subset of the entire domain. Once Δs_{edge} is specified, a few simple modifications to Eq. (6) are imposed to ensure that the resulting edge spacing meets this requirement. First, s_{s1}' and s_{c1}', the equilibrium positions of the torsion springs at the boundary, are reset to Δs_{edge}. The stiffness factor λ is increased slightly in this region to hold the points at these positions. To provide a smooth transition at the boundary, the differences $s_{s1}' - \Delta s_{\text{edge}}$ and $s_{c1}' - \Delta s_{\text{edge}}$ are then distributed into the adaptation domain by adjusting s_{si}' and s_{ci}', respectively, in a manner so as to ensure that they remain monotonically increasing.

Another precaution taken to ensure spacing continuity at the boundaries of the adaptation domain is to adjust the

weighting functions in this region. Since the product $w_i \Delta s_i$ is assumed constant along the grid line, the edge weighting function w_1 is redefined as $w_1 = P/\Delta s_{\text{edge}}$, where P is an average product $w_i \Delta s_i$ over the grid line. The surrounding weighting functions are then adjusted to provide a smooth transition.

Estimation of Solution Error

The selection of a solution error measure or weighting functions and the normalized flow variable $\bar{f}$ used to drive the grid adaptation is considered in this section. Ideally, it is desired to minimize the truncation error and distribute the error uniformly over the computational domain. The truncation error is generally proportional to $(\Delta s)^n \, \partial^n \phi / \partial s^n$ where n denotes the order of accuracy.

As in many of the studies on solution-adaptive gridding, a linear combination of gradients and curvature of selected dependent and/or physical variables is used here as weighting functions. Finding a flowfield variable that will consistently represent solution error in all regions of the solution domain is difficult, if not impossible. Some variables change very rapidly in certain regions, but remain fairly smooth in other regions where another variable could be undergoing severe change. In the present study, an algorithm developed earlier by Harvey et al.[8] is used to automatically choose which variables are to represent the weighting function at each grid point location. The scheme computes gradients and/or curvature of each user specified variable and then, after normalizing each of these, chooses the largest in magnitude to represent the weighting function at each point.

The normalized flow variable $\bar{f}_i$ at the ith point along the current coordinate line is computed as

$$\bar{f}_i = \frac{f_i - f_{\min}}{f_{\max} - f_{\min}} \tag{9}$$

where f_i is a linear combination of the gradients and curvature of the dependent flow variables ϕ_k:

$$f_i = \alpha \left(\frac{\partial \phi_i}{\partial s} \right) + \beta \left(\frac{\partial^2 \phi_i}{\partial s^2} \right)$$

where

$$\frac{\partial \phi_i}{\partial s} = \max_k \left| \frac{\partial \phi_i}{\partial s} \right|_k, \qquad \frac{\partial^2 \phi_i}{\partial s^2} = \max_k \left| \frac{\partial^2 \phi_i}{\partial s^2} \right|_k$$

for all specified ϕ_k, i.e., Mach number, pressure, density, etc. Hence, the gradients of all selected flow variables are computed, then the maximum is chosen to represent f_i at each point along the current adaptation line. The constants α and β are specified by the user. All numerical results of the following section were obtained using values of α and β equal to unity and zero, respectively.

Test Results

The three-dimensional solution-adaptive PNS algorithm is tested on the hypersonic flow over a 10-deg right-circular cone yawed in its symmetry plane at varying angles of freestream incidence α. The flowfield conditions were chosen to match those of the experimental study conducted by Tracy.[14] These conditions are $M_\infty = 7.95$ and $Re/\bar{l} = 0.414 \times 10^6$ with $\bar{l} =$ 0.1016 m (4 in.) as the total length of the cone. The freestream and wall temperatures are $T_\infty = 55.4$ K and $T_w = 309.8$ K and $\gamma = 1.4$, $Pr = 0.72$.

Results have been obtained for the flow over a circular cone at angles of incidence of 8, 16, and 24 deg using both solution-adaptive and fixed grids. For each of these cases, a conical starting solution was obtained at $x = 0.002$ m by employing a stepback procedure and using a fixed conical grid. After this starting solution was obtained, the solution-adaptive marching procedure was employed to a marching station corresponding to $x = 0.1016$ m for each of the three angle-of-incidence cases studied.

Quite frequently, optimum values of user parameters for adaptation in different crossflow directions can vary. For the 8- and 16-deg angle-of-incidence cases, the stiffness parameter λ of Eqs. (7) was given values of 0.2 and 2.0 for radial and circumferential adaptations, respectively. For the 24-deg angle-of-incidence case, the values of λ used were 0.5 and 5.0 for radial and circumferential adaptations, respectively. The orthogonality to straightness parameter in the streamwise direction C_s of Eq. (8) was given a value of 0.5 for all angle-of-incidence cases, whereas the crossflow orthogonality to straightness parameter C_c was given values of 0.5, 0.6, and 0.35 for the 8-, 16-, and 24-deg angle-of-incidence cases, respectively.

Mach number, pressure, and density are the three variables used in the weighting function selection procedure when adapting in the radial direction. For circumferential grid adaptations, the objective was to increase grid resolution on the leeward side of the cone in the circumferential direction. In an attempt to artificially resolve a region of the flowfield known to contain additional complexities, boundary-layer thickness was added to this list of adaptation variables when adapting circumferentially. At each circumferential grid point location, the boundary-layer thickness adjacent to the grid point was computed and normalized with respect to the maximum value. If this value at a point was greater than the gradients of the previously listed variables, then boundary-layer thickness was chosen as the weighting function at that point [i.e., boundary-layer thickness was included as the kth value of $|\partial \phi_i / \partial s|_k$ of Eq. (9)]. The maximum value of boundary-layer thickness occurs at the leeward meridian for a cone at angle of incidence, whereas the maximum circumferential pressure gradient occurs closer to the windward meridian. The net effect of using boundary-layer thickness when adapting in the circumferential direction was a slight increase in the grid resolution at the leeward side of the cone compared to cases that did not include the boundary-layer thickness as an adaptation variable. Additional discussion on the present use of boundary-layer thickness to control grid point movement will be provided in the following sections.

Adaptation sweeps were performed in both crossflow directions at each marching station. The circumferential sweep at each marching station was performed by starting at the cone surface and moving outward. However, the direction of the radial sweeps alternated, sweeping one crossflow surface from the windward to leeward meridian and the next surface from leeward to windward, etc. These alternating direction sweeps in the radial direction permit information to propagate from both directions, contributing additional smoothness to the grid.

Grids and Contour Plots

8-Degree Yaw Angle

For the 8-deg angle-of-incidence case, a 65×65 crossflow grid was used for both fixed and solution-adapted cases. Figure 2 illustrates a sectional view of the resulting solution-adapted computational grid. Grid point clustering is observed at the bow shock location as well as in the boundary layer from the windward to the leeward side of the cone. For this case, the angle of incidence is less than the cone angle; thus, the boundary layer remains attached up to the leeward meridian in the crossflow plane. However, the boundary layer thickens as the flow moves toward the leeward meridian in the crossflow direction, and as this thickening progresses, the grid adaptation supplies the boundary layer with additional grid points.

Figure 3 shows contours of constant Mach number at an x location of $x = 0.1016$ m. Improvements in bow shock resolution are observed in the solution obtained using the adapted grid over that of the fixed grid. The inverted triangle symbols

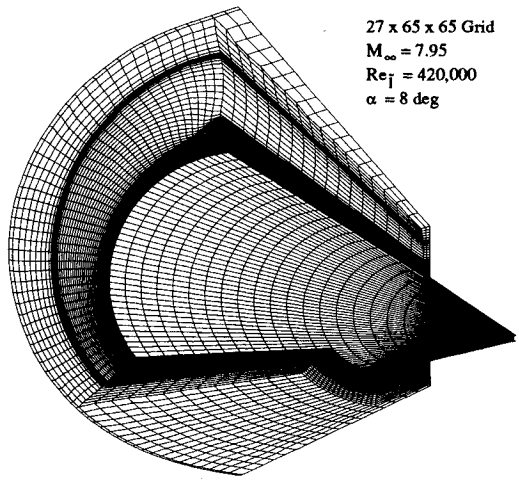

Fig. 2 Sectional view of solution-adapted computational grid.

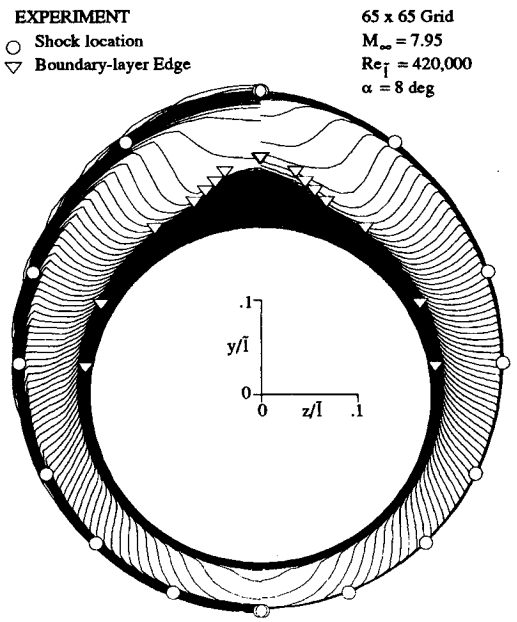

Fig. 3 Comparison of Mach number contours at $x = 0.1016$ m: left half, fixed grid; right half, solution-adapted grid.

of this figure indicate the boundary-layer edge deduced experimentally by Tracy,[14] whereas the circles indicate experimentally determined shock wave location. The locations of these features, as observed by Tracy,[14] are well predicted by the solution-adaptive PNS solver.

16-Degree Yaw Angle

A 70×70 crossflow grid was employed for both fixed and adapted cases at a 16-deg angle of yaw. Figure 4 shows a sectional view of the resulting solution-adapted grid for this case. This figure illustrates the true three-dimensional nature of the present problem. Each crossflow plane has been adapted in both crossflow directions. The torsional influence in the streamwise direction has prevented relative skewness between adjacent crossflow planes, permitting the marching process to proceed without interruption. The position of the bow shock surface is marked by the outermost grid clustering that extends around the entire figure. Also evident in this figure is a gradual thickening of the clustering region near the cone surface in the circumferential direction illustrating the cross-stream structure of the boundary layer. Its point of separation from the cone surface is marked by the breakup of this grid clustering region. The grid points remain clustered in the detached viscous layer until a second division of the clustering region occurs where the flow rolls up into a vortical-like structure.

For the 16-deg angle-of-incidence case, the radial adaptation process at each marching station was performed by sweeping grid lines from the windward meridian to the leeward meridian. On the other hand, for the 8-deg angle-of-incidence case, the direction of radial adaptation sweeps was alternated at each successive marching station as described earlier. The absence of alternating direction adaptations can cause a slight waviness to appear in the grid, as seen in the leeward symmetry plane of Fig. 4. This waviness is not present in the grid of Fig. 2 where the alternating direction technique was employed.

When the angle of incidence is increased from 8 to 16 deg, it becomes greater than the cone half-angle and, as a result, a region of crossflow separation develops on the leeward side of the cone where the viscous layer detaches from the cone surface. This separation results from the increasingly adverse crossflow pressure gradient on the leeward side of the cone. A rotational feature in the flowfield is evident in the solution-

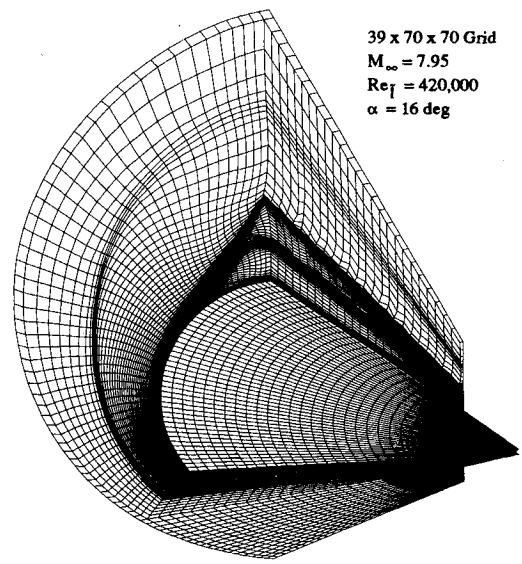

Fig. 4 Sectional view of solution-adapted computational grid.

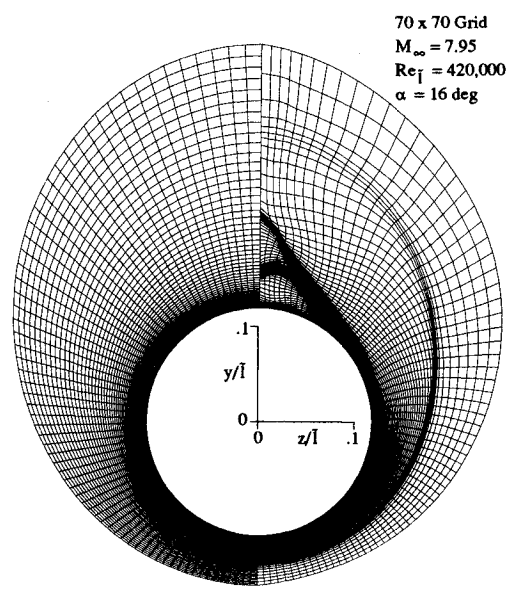

Fig. 5 Comparison of crossflow computational grids at $x = 0.1016$ m: left half, fixed grid; right half, solution-adapted grid.

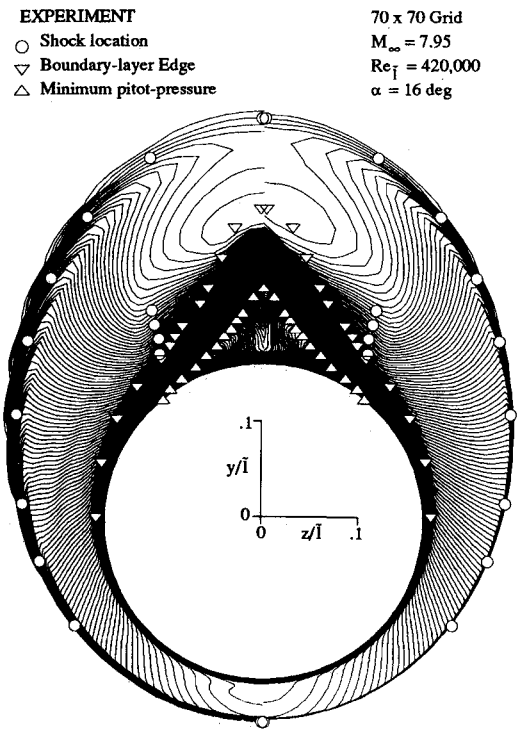

Fig. 6 Comparison of Mach number contours at $x = 0.1016$ m: left half, fixed grid; right half, solution-adapted grid.

adapted mesh shown on the right half of Fig. 5. Increased grid clustering is observed around the bow shock region and detached shear layer. The clustering region on the leeward side of the cone and situated about halfway between the top of the detached shear layer and the cone surface is due to the circumferential grid lines attempting to roll up and imitate the shape of the existing crossflow vortical structure.

The experiments of Tracy[14] detect weak embedded crossflow shock waves at the onset of the separation region where the Mach number due to the cross-stream velocity components exceeds unity. The experimentally observed positions of these embedded shocks in addition to the bow shock position are illustrated by the overlaid circles of Fig. 6. Again, excellent agreement in the experimentally observed position and the computed position of the bow shock is observed for both the fixed and adapted grid solutions. The Mach contours of Fig. 6 also show improved resolution of the bow shock for the solution-adapted case over the fixed grid case. However, the embedded shocks are not evident in the Mach contours of this figure due probably to their relative weak strength. The inverted triangle and triangle symbols of Fig. 6 show the locations of the outer and inner edges, respectively, of the detached viscous layer. These experimental data were deduced from the pitot pressure measurements of Tracy.[14]

24-Degree Yaw Angle

When the angle of incidence is further increased to 24 deg, additional thickening of the separated region occurs at the leeward side of the cone. The viscous layer starts out running along the cone surface in the circumferential (crossflow) direction. Close to the leeward side it separates from the surface and turns sharply upward becoming vertical, running parallel to the leeward symmetry plane and away from the cone surface. The detached viscous layer then turns sharply back toward the symmetry plane, intersecting normal to it. Because of the abrupt changes in the direction of this shear layer, the adaptive grid algorithm has to choose which family of coordinate lines is best suited to resolve this shear layer while simultaneously maintaining a sufficient degree of orthogonality.

Figure 7 shows a grid comparison for the fixed (left-half) and solution-adapted (right-half) cases, each side consisting of a 90×90 grid. Grid point clustering is observed where the viscous layer detaches from the cone surface and turns upward. Before this change in direction, the viscous layer is running essentially parallel to the circumferential family of grid lines and can easily be resolved by them. However, following its detachment, the viscous layer turns almost normal to circumferential lines, making it difficult for them to adjust and, due to orthogonality restrictions, disallows any significant resolution from coordinate lines of the opposite family. This lifting of the circumferential lines also causes the radial lines to bend inward, away from the symmetry plane, leaving less grid resolution in this region.

Mach number contours are plotted in Fig. 8 for both the fixed grid (left-half) and adapted (right-half) cases at a 24-deg

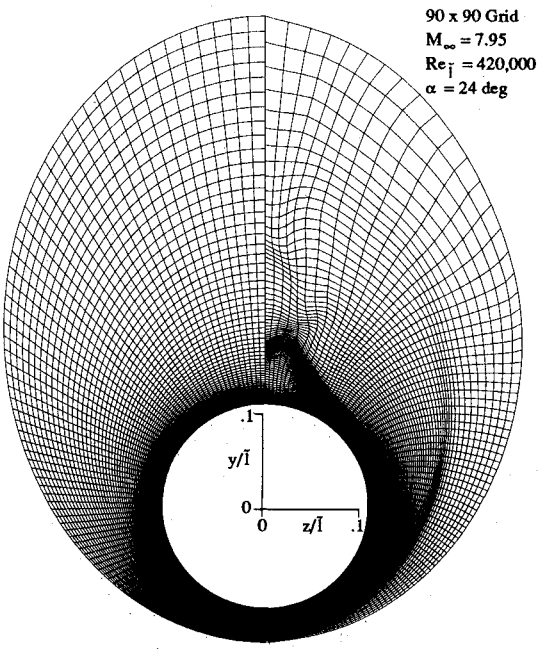

Fig. 7 Comparison of crossflow computational grids at $x = 0.1016$ m: left half, fixed grid; right half, solution-adapted grid.

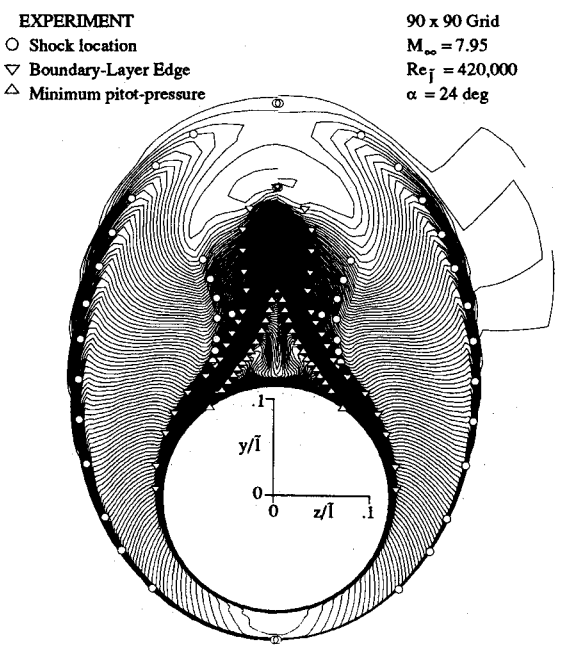

Fig. 8 Comparison of Mach number contours at $x = 0.1016$ m: left half, fixed grid; right half, solution-adapted grid.

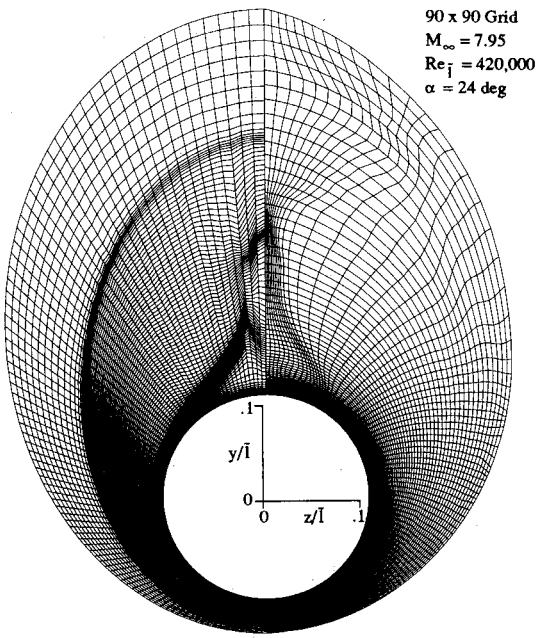

Fig. 9 Comparison of crossflow computational grids at $x = 0.1016$ m: left half, adapted in radial direction only; right half, adapted in circumferential direction only.

yaw angle. The overlaid circles represent shock wave positions as observed experimentally by Tracy.[14] The inverted triangles and triangles represent the outer and inner edges, respectively, of the shear layer as deduced from the pitot pressure measurements of Tracy.[14] An increase in resolution of the top of the shear layer can be seen in the adapted side of this figure, although this increase in resolution is less apparent for the portion of the shear layer that runs almost vertically upward. This loss of resolution is due to rather strict orthogonality constraints imposed on the grid.

In an attempt to resolve as much of the detached shear layer on the leeward side of the cone as possible, solution-adaptive calculations were performed by adapting the grid in each crossflow direction separately. The resulting grid for the radial adaptations is illustrated by the left half of Fig. 9, whereas the right half resulted from adapting in the circumferential direction only. As in Fig. 7, both halves of this figure consist of a 90×90 computational grid. Figure 9 illustrates how each coordinate line family resolves the detached shear layer while simultaneously attempting to maintain a minimum degree of grid orthogonality. For the radial adaptations (left half of Fig. 9), grid lines on the leeward side of the cone must first turn sharply away from the cone surface and then turn back normal to the leeward meridian in order to resolve the detached shear layer all the way to the top. Some of the grid orthogonality is lost due to these sharply turning circumferential lines of the left half of Fig. 9, more so in the region where the detached shear layer becomes almost normal to the cone surface. The radial adaptations alone (left half of Fig. 9) did very well in clustering grid points in the bow shock location. The resulting crossflow grid is accurately aligned with the bow shock the entire length of the grid, from windward to leeward meridians. This increase in alignment and resolution throughout the grid of Fig. 9 (left side) resulted from performing the radial adaptations using the alternating direction sweeping technique, which allows for information to propagate from both sides of the grid (windward and leeward meridians).

About halfway between the top of the shear layer and the cone surface at the leeward meridian, another grid clustering region exists inside the detached shear layer. This same type of grid structure was also observed in Figs. 5 and 7 at about the same location.

The circumferential only adaptations in the right half of Fig. 9 illustrate improvements in circumferential grid resolution at the leeward symmetry plane over the multidirectional adaptations of Fig. 7. The reason for this behavior can best be explained with a discussion on the manner in which flowfield gradients used in constructing the weighting functions are computed. The derivatives are computed in the direction of the grid line. In the present test cases, as a result of the radial grid adaptation sweep, circumferential grid lines tend to align themselves with the detached shear layer at the leeward side of the cone. Consequently, when the circumferential adaptation sweep is performed, the weighting function is computed as a derivative in the direction of the grid line (no longer in a strict circumferential orientation), which runs parallel with the shear layer. For the circumferential only adaptations of Fig. 9, the positions of the circumferential grid lines were not disturbed by radial adaptations and, unlike the multidimensional adaptation cases, cut directly through the shear layer, in a direction of strong flowfield gradient. When adapting in both directions simultaneously, the circumferential grid lines become parallel with the detached shear layer, along which there are no strong gradients to use as weighting functions. This is another reason the authors opted to modify the weighting function with boundary-layer thickness for circumferential adaptations when adapting in both crossflow directions simultaneously.

No improvements are seen in the grid resolution in the vicinity of the bow shock due to the lack of radial adaptations. For each half of Fig. 9, the grid can be seen to cluster around the separated shear layer all the way to the top, as desired.

Figure 10 shows Mach contours overlaid with the symbols as in the previous angle-of-incidence cases. The left half of this figure shows improvements in bow shock resolution over all of the 24-deg angle-of-incidence cases presented thus far. The detached shear layer in both halves of Fig. 10 (unidirectional adaptations only) is more clearly resolved than in either half of Fig. 8 (fixed grid or multidirectional adaptation cases). The increased circumferential resolution provided by the circumferential only adaptations (right half of Fig. 10) allows for a more clearly defined viscous layer, which extends slightly higher than the viscous layer predicted with the fixed grid.

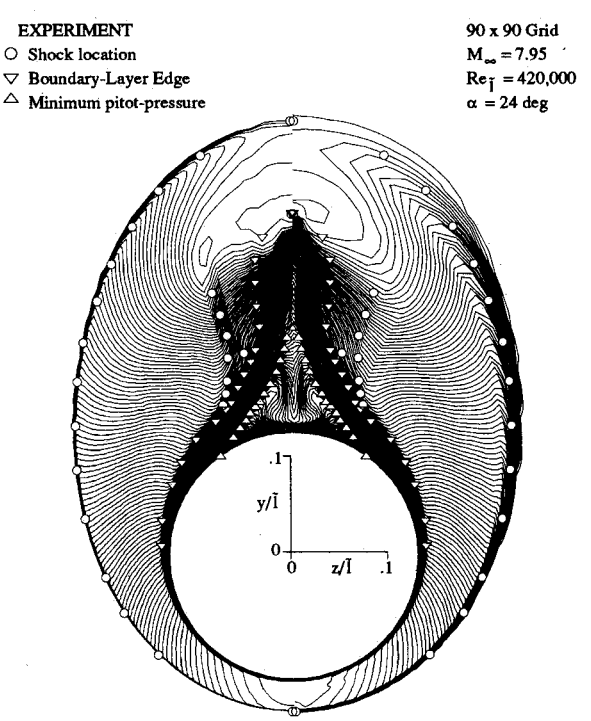

Fig. 10 Comparison of Mach number contours at $x = 0.1016$ m: left half, adapted in radial direction only; right half, adapted in circumferential direction only.

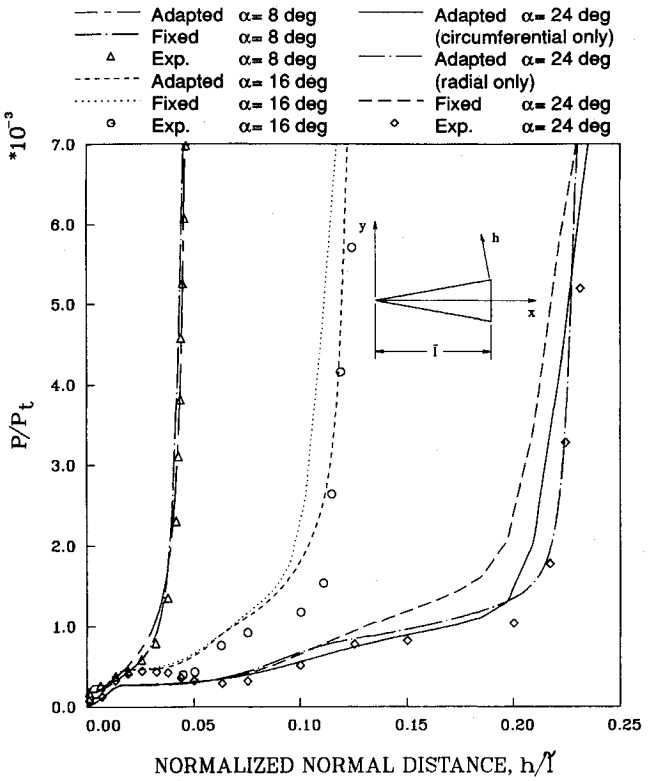

Fig. 11 Comparison of pitot pressure profiles at leeward meridian.

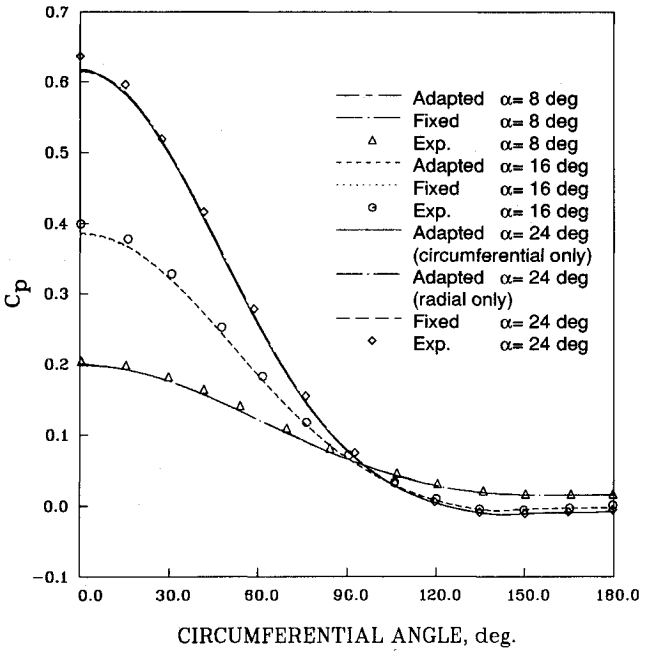

Fig. 12 Circumferential surface pressure distributions at $x = 0.1016$ m.

This same degree of resolution is also observed using radial adaptations alone (left half of Fig. 10), although a slight waviness exists in the vertical portion of the shear layer due to the lack of grid orthogonality in this region. The inner portion of the viscous layer that was predicted with either of the unidirectional adaptations of Fig. 10 is more clearly defined than that predicted using either the fixed grid or the multidirectional adaptations of Fig. 8.

No significant improvement can be detected in the resolution of the embedded shock waves, even with the use of the adaptive grid. This is due primarily to an insufficient number of radial grid lines available to cluster in these regions. For circumferential adaptations alone, all available grid points move toward the shear layer, leaving less grid resolution in embedded shock regions. These embedded shock waves as observed by Tracy[14] are indicated by the overlaid circles emanating from the detached portion of the shear layer in a lambda shaped pattern.

Pressure and Mach Number Comparisons

Figure 11 shows a comparison of pitot pressure profiles in the leeward meridian plane for all three angle-of-incidence cases using both solution-adapted and fixed grids with experimental results obtained by Tracy.[14] The results for the solution-adapted cases show improvements over the fixed grid cases at all angles of incidence. The experiments show an abrupt increase in the pitot pressure at the inner edge of the detached shear layer. The solution-adapted 24-deg angle-of-incidence cases predict this feature in the shape of the pitot pressure profile fairly well. The 24-deg fixed grid solution predicts a more gradual rise in pitot pressure through the detached shear layer. The solution-adaptive PNS solver underpredicts the slight bulge in pitot pressure that exists near the cone surface. One possibility that may improve the prediction of this feature is to adapt the points on the surface of the cone, thus allowing for a finer circumferential grid resolution near the cone surface. In all cases presented for this work, the surface points were not permitted to move. Because of orthogonality constraints at the surface, the movement of grid points a small distance above the surface was limited, disallowing further circumferential grid refinement. Pitot pressure predictions for the 24-deg cone case using multidirectional adaptation sweeps were found to be only slightly better than those predicted using the fixed grid and are not included in Fig. 11.

Figure 12 compares circumferential pressure distributions with those obtained experimentally by Tracy[14] at a marching station corresponding to $x = 0.1016$ m. The results computed with the solution-adaptive PNS solver agree very well with experiment; agreement is not significantly influenced by the adaptation of the grid.

Figure 13 compares Mach number profiles at the leeward meridian in the bow shock region for each cone case. Slight improvements can be seen in the resolution of the bow shock for the 8- and 24-deg (radial only) adapted cases. The 16-deg

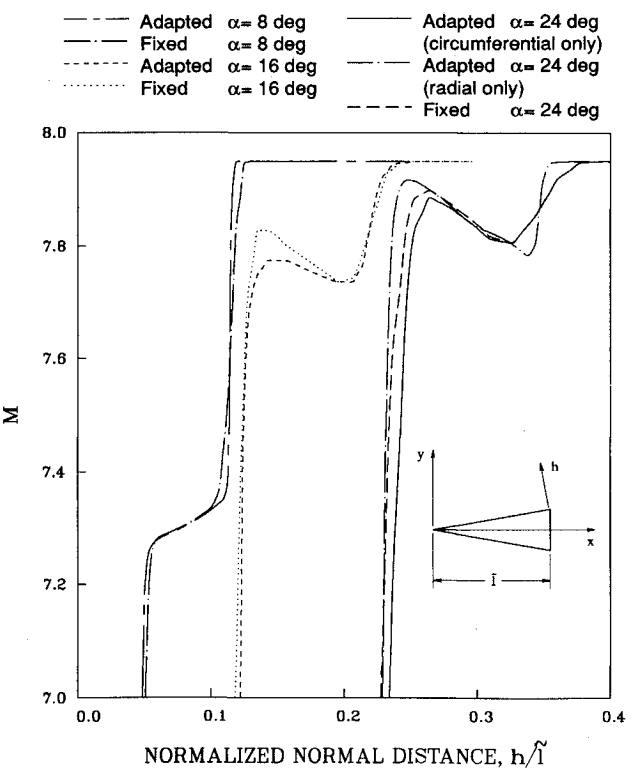

Fig. 13 Comparison of Mach number profiles at leeward meridian.

angle-of-incidence case shows less improvement due to the lack of grid resolution in this region (see Fig. 5) due primarily to the lack of alternating direction sweeps for this case as discussed in a previous section. In adapting the grid for the 16-deg cone case, the radial adaptations were performed by sweeping lines from windward to leeward only. For the 8- and 24-deg (radial only) cases, the alternating technique discussed earlier was employed, allowing information to propagate from both leeward and windward sides of the cone.

Concluding Remarks

A three-dimensional solution-adaptive grid procedure has been developed and used with a parabolized Navier-Stokes solver. The method of grid adaptation involves the efficient redistribution of grid points along each computational coordinate line using an equidistribution concept. Grid point motion is bounded so as to prevent excessive grid skewness and allow for uninterrupted recomputation of the flowfield on a smooth adapted marching surface. The adaptive grid algorithm provides improved shock resolving characteristics over the conventional flow algorithm and exhibits the ability to align grid lines with existing flowfield structure. However, as the 24-deg angle-of-incidence cone case indicates, the present multidirectional adaptive grid method experiences difficulty resolving flowfields where flow structure changes direction abruptly. When one family of computational coordinates is aligned with a flow structure that is changing direction very rapidly, it becomes difficult for the opposite family of coordinates to align with the same structure and still maintain grid orthogonality. It has been demonstrated that the use of the solution-adaptive algorithm significantly enhances the prediction of pitot pressure on the leeward side of cones at various angles of incidence. The surface pressure is unaffected by the adaptation of the grid, due primarily to the relative fine clustering of the fixed grid in this region.

Acknowledgments

This work was supported by the Applied Computational Fluids Branch at NASA Ames Research Center under Joint Interchange NCA2-326 and under Branch Chief Terry L. Holst. This support is gratefully acknowledged.

References

[1]Thompson, J. F., "A Survey of Dynamically-Adaptive Grids in the Numerical Solution of Partial Differential Equations," *Applied Numerical Mathematics,* Vol. 1, North-Holland, Amsterdam, The Netherlands, Jan. 1985, pp. 3–27.

[2]Hawken, D. F., "Review of Adaptive-Grid Techniques for the Solution of Partial Differential Equations," Univ. of Toronto, Toronto, Ontario, Canada, Inst. for Aerospace Studies, Review 46, Dec. 1985.

[3]Nakahashi, K., and Deiwert, G. S., "A Self-Adaptive Grid Method with Application to Airfoil Flow," AIAA Paper 85-1525, Cincinnati, OH, July 1985.

[4]Nakahashi, K., and Deiwert, G. S., "Three-Dimensional Adaptive Grid Method," *AIAA Journal,* Vol. 24, No. 6, 1986, pp. 948–954.

[5]Gnoffo, P. A., "A Vectorized, Finite-Volume, Adaptive Grid Algorithm Applied to Planetary Entry Problems," AIAA Paper 82-1018, June 1982.

[6]Davies, C. B., and Venkatapathy, E. W., "A Simplified Self-Adaptive Grid Method, SAGE," NASA TM-102198, Oct. 1989.

[7]Djomehri, D. J., and Deiwert, G. S., "Three-Dimensional Self-Adaptive Grid Method for Complex Flows," NASA TM-101027, Nov. 1988.

[8]Harvey, A. D., Acharya, S., Lawrence, S. L., and Cheung, S., "Solution Adaptive Grid Procedure for High-Speed Parabolic Flow Solvers," *AIAA Journal,* Vol. 29, No. 8, 1991.

[9]Lawrence, S. L., "Application of an Upwind Algorithm to the Parabolized Navier-Stokes Equations," Ph.D. Dissertation, Iowa State Univ., Ames, IA, May 1987.

[10]Lawrence, S. L., Tannehill, J. C., and Chaussee, D. S., "Application of an Upwind Algorithm to the Three-Dimensional Parabolized Navier-Stokes Equations," AIAA Paper 87-1112, Honolulu, HI, June 1987.

[11]Roe, P. L., "Approximate Riemann Solvers, Parameter Vectors, and Difference Schemes," *Journal of Computational Physics,* Vol. 43, 1983, pp. 357–372.

[12]Vigneron, Y. C., Rakich, J. C., and Tannehill, J. C., "Calculation of Supersonic Viscous Flow over Delta Wings with Sharp Subsonic Leading Edges," AIAA Paper 78-1137, July 1978.

[13]Chakravarthy, S. R., and Szema, K. Y., "An Euler Solver for Three-Dimensional Supersonic Flows with Subsonic Pockets," AIAA Paper 85-1703, July 1985.

[14]Tracy, R. R., "Hypersonic Flow over a Yawed Circular Cone," Graduate Aeronautical Labs., California Inst. of Tech., Pasadena, CA, Memorandum 69, 1963.